

PAPER

# Monodispersed ZnO nanoink and ultra-smooth large-area ZnO films for high performance and stable organic solar cells

To cite this article: Jingbo Guo *et al* 2022 *Flex. Print. Electron.* **7** 025013

View the [article online](#) for updates and enhancements.

## You may also like

- [Heterojunction Solar Cells Fabricated with a  \$\text{Cu}\_2\text{O}/\text{Mn}\$  Thin Film Grown Epitaxially on p-Type  \$\text{Cu}\_2\text{O}/\text{Na}\$  Sheets By Electrochemical Deposition](#)  
Kyosuke Watanabe, Ryouzuke Uozaki, Jouji Yamazaki et al.
- [Silk protein as a new optically transparent adhesion layer for an ultra-smooth sub-10 nm gold layer](#)  
Kyungtaek Min, Muhammad Umar, Shinyoung Ryu et al.
- [Atomistic model of ultra-smooth amorphous thin film growth by low-energy ion-assisted physical vapour deposition](#)  
R Alvarez, L Vazquez, R Gago et al.



The Electrochemical Society  
Advancing solid state & electrochemical science & technology

243rd ECS Meeting with SOFC-XVIII

Boston, MA • May 28 – June 2, 2023

**Abstract Submission Extended  
Deadline: December 16**

[Learn more and submit!](#)

# Flexible and Printed Electronics



## PAPER

# Monodispersed ZnO nanoink and ultra-smooth large-area ZnO films for high performance and stable organic solar cells

RECEIVED  
5 February 2022

REVISED  
6 May 2022

ACCEPTED FOR PUBLICATION  
13 May 2022

PUBLISHED  
26 May 2022

Jingbo Guo<sup>1,2</sup>, Yunfei Han<sup>2</sup>, Zihan Xu<sup>2</sup>, Wusong Zha<sup>2</sup>, Jin Fang<sup>2</sup>, Qun Luo<sup>2,\*</sup> , Liqi Liu<sup>1,\*</sup> and Chang-Qi Ma<sup>2</sup> 

<sup>1</sup> School of Materials Science and Engineering, Shanghai University, Shanghai 201900, People's Republic of China

<sup>2</sup> i-Lab & Printable Electronics Research Center, Suzhou Institute of Nano-Tech and Nano-Bionics, Chinese Academy of Sciences (CAS), Suzhou 215123, People's Republic of China

\* Authors to whom any correspondence should be addressed.

E-mail: [qluo2011@sinano.ac.cn](mailto:qluo2011@sinano.ac.cn) and [llq@shu.edu.cn](mailto:llq@shu.edu.cn)

**Keywords:** monodispersed ZnO, nanoink stability, ZnO electron transporting layer, slot-die coating, organic solar cells

Supplementary material for this article is available [online](#)

## Abstract

In the organic solar cells (OSCs), zinc oxide nanoparticles (ZnO NPs) have been widely used to fabricate electron transporting layer (ETL). However, spontaneous aggregation of NPs and film surface defects are two issues that limit the application of ZnO NPs in the printed photovoltaics. To simultaneously solve the two problems, the ZnO nanoinks were modified with a 2-(2-methoxyethoxy) acetic acid (MEA) solution, in which a monodispersed nanoink was obtained, and no aggregation occurred after 18 months of storage at room temperature. Meanwhile, the ZnO:MEA ETL had fewer surface hydroxyl groups defects because of Lewis acid-base interactions. The monodispersibility and passivated surface defects ensured an ultra-smooth ZnO film, leading to an improved device performance, longer lifetime, and higher thickness tolerance. As a result, an efficiency of 15.84% was achieved for the 1 cm<sup>2</sup> PM6:Y6 ZnO:MEA ETL-based OSCs, and the  $T_{80}$  lifetime was also increased to 6600 h. The thickness of ZnO:MEA ETL could be increased to 225 nm with less performance degradation. ZnO:MEA NPs were dispersed well in alcohols with high boiling points, which ensured a high-quality slot-die coated film. The ZnO:MEA ETL also has a unique advantage in flexible organic OSCs, with enhanced bending resistance during 10000 times bending. These properties demonstrated the great potential of ZnO:MEA nanoinks in the printed electronics.

## 1. Introduction

Organic solar cells (OSCs) are regarded as potential energy harvesting devices for various portable and wearable electronics because of their lightweight, flexible, roll-to-roll (R2R) printing compatibility, and high absorption coefficient under the illumination of indoor light-emitting diode lamps. The power conversion efficiency (PCE) of OSCs has been significantly improved because of the development of materials, phase separation morphology control, and interface optimization. Thus far, the maximum efficiency of OSCs has reached 19% [1–5], showing great potential for commercialization and industrialization. The inverted structure of OSCs were considered to be more stable than the conventional devices since the no acidic poly(3,4-ethylenedioxythiophene)-poly(styrenesulfonate) hole transporting layer was

used and the oxidation of low-work-function metal electrodes could be avoided [6].

Zinc oxide (ZnO) is commonly used as electron transporting layer (ETL) in the inverted OSCs because of its non-toxic, earth-abundant, low-cost, and multiple solution-processable routes. For the conventional low-temperature processed ZnO nanoparticles (ZnO NPs) synthesized through chemical reaction of zinc salt and hydroxide [7], the surface of ZnO NPs is naturally surrounded by hydroxy surface ligands [8]. These hydroxy groups outside ZnO NPs would cause severe aggregation, which makes the ink unstable. In addition, films fabricated from aggregated nanoparticles are always rough, which would generate high charge transport resistance between ETL and the active layer [9, 10], consequently influencing device performance. In particular, the smaller spread force during printing than

in spin-coating would result in worse interface contact [11–13]. Several approaches have been developed to address this problem, such as titanium diisopropoxide bis(acetylacetonate) ( $\text{Ti}(\text{acac})_2$ ) [14]. Wei *et al* modified ZnO nanoparticles with poly(ethylene imine) (PEI) [15, 16] and capped ZnO nanoparticles with silane [17]. Yi *et al* [18] and Ambade *et al* [19, 20] found in ZnO:PEI nanoparticles, 2-(2-methoxyethoxy) acetic acid (MEA) could prevent aggregation of ZnO NPs. Additionally, previous works have shown that both the device efficiency and stability are highly affected by the surface defects of the ZnO ETL [21–26]. The film defects would trap electrons and aggravate the interface charge recombination, which decreased the performance [27–30]. Meanwhile, the existence of surface hydroxy groups aggravated the photocatalytic effect of ZnO, causing catastrophic degradation of small-molecule acceptors and leading to poor device stability [27, 31]. Modifying ZnO films with small molecules or treating the films with acid solution [24–26, 32, 33] have been developed to solve this problem. Although these approaches were effective in improving ink stability or passivating surface defects, the underlying reason of aggregation has not been studied yet. In addition, although previous studies have demonstrated that several strategies are effective in passivating film defects through surface modification and improving ink stability through chemical grafting, few approaches can simultaneously solve these two issues. In terms of colloidal chemistry, both the aggregation of nanoparticles and film defects might originate from the surface charge effect, which is highly affected by the pH environment of the inks and steric hindrance effect between the nanoparticles [34–37].

Here, we systematically investigated the effect of pH environment on ink dispersibility by treating nanocrystals with acid and alkali solutions. Acid hybrid ZnO inks have good monodispersity and long-term ink stability, which enabled the formation of ultra-smooth ZnO films and enhanced electron transport. Therefore, the ZnO:MEA ETL-based  $1\text{ cm}^2$  PM6:Y6 OSCs showed a performance of 15.9%, and a  $T_{80}$  lifetime of 6600 h. The ZnO:MEA ETL also contributed to the improved mechanical properties of the flexible OSCs, which kept 88% of initial efficiency after 10 000 bending cycles. Using the monodispersed ZnO nanoinks, large-area ( $10 \times 10\text{ cm}^2$ ) films were fabricated through slot-die coating and showed excellent homogeneity. These characteristics strongly suggested the great advantages of ZnO:MEA for printed electronics.

## 2. Experimental section

### 2.1. Materials

Both electron donor PM6, poly[[4,8-bis[5-(2-ethylhexyl)-4-fluoro-2-thienyl]benzo[1,2-*b*:4,5-*b'*:4,5-eth

ylhexyl)-4-fluoro-2-thiophenediyl[5,7-bis(2-ethylhexyl)-4,8-dioxo-4*H*,8*H*-benzo-[1,2*c*:4,5*c'*:4,5*z*o-hexyl)-4,8-dioxo-4-2-thienyl]benz *c* (PM6), and electron acceptor Y6, (2,20-((2*Z*,20*Z*)-((12,13-bis(2-ethylhexyl)-3,9-diundecyl-12,13-dihydro-[1,2,5]thiadiazolo-[3,4-*e*] thieno[2[thienhexyl]-3,9-o[20,30:4,5]pyrrolo[3,2-*g*]-thieno[20,30:4,5]thieno[3,2-*b*]indole-2,10-diyl)bis(methanylylidene))bis(5,6-difluoro-3-oxo-2,3-dihydro-1*H*-inden-2,1-diylidene))dimalononitrile) were purchased from Solarmer Materials Inc., Beijing. 1-chloronaphthalene was purchased from Sigma-Aldrich.  $\text{Zn}(\text{OAc})_2 \cdot 2\text{H}_2\text{O}$ , KOH, and tetramethylammonium hydroxide (TMAH) were purchased from J&K Scientific Ltd. MEA, methanol (MeOH), ethanol (EtOH), isopropyl alcohol (IPA), *n*-butanol (BuOH), and ethylene glycol monomethyl ether (EGME) were purchased from Adamas.

### 2.2. Synthesis of the nanoinks

ZnO NPs were synthesized through the similar route as previously reported [7]. The ZnO NPs were washed twice using methanol and then dispersed in different alcohol solvents, like MeOH, EtOH, IPA, BuOH, and EGME through ultrasonication, and finally ZnO nanoinks with concentration of  $15\text{ mg ml}^{-1}$  were obtained. The acid or base treated ZnO was prepared by adding MEA and TMAH solution into the ZnO nanoink, respectively.

### 2.3. Characterization of the nanoinks and films of ZnO

Transmission electron microscopy (TEM) images were measured using Tecani G2 F20 S-Twin (EEI). X-ray diffractometer (XRD) of ZnO powder was performed using a D8 Advance from Bruker AXS. X-ray photoelectron spectroscopy (XPS) were carried out using an ultrahigh-vacuum surface analysis system (Kratos AXIS Ultra DLD, SINANO). Dimension 3100 (VEECO) was used to measure the atomic force microscopy (AFM) images. Zetasizer Nano (Malvern) was taken to measure the diameter and Zeta potential of the ZnO nanoinks. The pH values were measured by the PHS-3E (INESA Shanghai). The profiler (DEKTAK 150, VEECO) was taken to characterize film thickness. Absorption spectra (UV-vis) were measured by Lambda 750 spectrometer (PerkinElmer). Photoluminescence (PL) characterization was carried out using Princeton instruments SP2500i under excitation of 330 nm.

### 2.4. Slot-die coating of large-area ZnO and ZnO:MEA films

The desktop-level multi-functional coating machine (Hunan Nano UP Electronics Technology Co., Ltd) was used for slot-die coating. The slot-die coated ZnO and ZnO:MEA films were prepared from ZnO and ZnO:MEA nanoinks ( $60\text{ mg ml}^{-1}$  in BuOH) on the

Ag nanowires (AgNWs) electrode. The speed of slot-die coating and temperature was  $10.0 \text{ mm s}^{-1}$  and  $50 \text{ }^\circ\text{C}$ , respectively.

## 2.5. OSC fabrication

To fabricate the inverted OSCs with a structure of glass/indium tin oxide (ITO)/ZnO ETL/PM6:Y6/MoO<sub>3</sub>/Al, the glass/ITO electrodes were firstly cleaned by ultrasound in deionized water, acetone, and IPA for half hour each step. After 10 min of UV ozone treatment, the ZnO, ZnO:MEA, and ZnO:TMAH ETLs were prepared from the nanoinks with spinning-coating speed of 2000 rpm. These films were subsequently annealed for 10 min at  $130 \text{ }^\circ\text{C}$ . Then, the active layer was prepared through spin-coating from the precursor solutions that composed of PM6, Y6 with concentration of 7.0 and  $8.4 \text{ mg ml}^{-1}$ , respectively. The solution was stirred continuously for 3 h at  $50 \text{ }^\circ\text{C}$  in prior spin-coating. Then, the PM6:Y6 active layers were prepared on ETLs through dynamic spin-coating at 2000 rpm for 60 s. The annealing condition of active layers was  $100 \text{ }^\circ\text{C}$  for 10 min. At last, 10 nm MoO<sub>3</sub> and 100 nm Al were deposited in successively thermal evaporated at a vacuum level around  $1 \times 10^{-5} \text{ Pa}$ . For the flexible organic solar cells (FOSCs), gravure printed polyethylene terephthalate (PET)/AgNWs were used as electrodes.

## 2.6. OSC characterization

Current density–voltage ( $J$ – $V$ ) characteristics was measured using a source meter (Keithley 2400) under AM 1.5 ( $100 \text{ mW cm}^{-2}$ ) illumination solar simulator (Zolix SS150) in the glove box. The external quantum efficiency (EQE) spectra were recorded by the homemade instrument. In detail, the instrument contained a tungsten halogen lamp (Osram64610), a monochromator (Zolix, Omni- $\lambda$ 300), a lock-in amplifier and an  $I$ – $V$  converter. Electrochemical impedance spectroscopy (EIS) were measured through PGSTAT 302N (Autolab). For long-term stability, the device was continuously illuminated in the glove box, and the performance was periodically recorded using the decay test system (PVLIT-G8001M, Suzhou D&R Instruments Co. Ltd) [27, 38]. The bending durability tests of FOSCs were carried out through FlexTest-F-C instrument (Hunan Nasheng Electronic Technology Co., LTD), and the bending radius was 5.0 mm.

## 3. Results and discussion

### 3.1. Physical properties of acid and base modified ZnO NPs

The pristine ZnO NPs were synthesized from the method of Moussodia [7]. By adding MEA and TMAH to the pristine ZnO nanoinks, the impact of pH on physical properties of ZnO

NPs was studied. Based on the absorbance spectra shown in figure S1 (available online at [stacks.iop.org/FPE/7/025013/mmedia](https://stacks.iop.org/FPE/7/025013/mmedia)), we ensured neither MEA nor TMAH modification has corroded ZnO. It is reasonable since the pH values of the nanoinks varied from 7.8 to 6.0 and 8.4 with the addition of MEA and TAMH, respectively. The mild change of pH condition caused no obvious reaction between ZnO and acid/base though ZnO is an amphoteric metal oxide. TEM images of these nanoparticles were then recorded to investigate their size. As shown in figures 1(a)–(c), we found that both ZnO and ZnO:TMAH nanoparticles had obvious aggregation, and the aggregation clusters of ZnO:TMAH were much larger than those of the ZnO nanoinks. In contrast, the ZnO:MEA nanoparticles were more homogeneous than the ZnO and ZnO:TMAH nanoparticles. From the high resolution transmission electron microscope (HRTEM) images (inset of figures 1(a)–(c)), particle sizes of ZnO:MEA and ZnO:TMAH NPs were determined to be  $7.2 \pm 0.4$  and  $7.4 \pm 0.3 \text{ nm}$ , which were like that of ZnO ( $7.6 \pm 0.3 \text{ nm}$ ) (figure 1(d)).

The crystallinity of the different ZnO nanocrystals was measured using XRD patterns (figure 1(e)). All of the obtained ZnO NPs showed a wurtzite structure with typical diffraction peaks corresponding to hexagonal ZnO (ICCD No. 21-1486) [17]. ZnO and ZnO:TMAH had sharp diffraction peaks and narrow half-peak widths, indicating good crystallinity and large grain size, while the diffraction peaks of ZnO:MEA were much wider.

The effects of acid/base modifications were investigated by PL spectroscopy under the excitation of 330 nm. As shown in figure 1(f), ZnO NPs have an emission peak at 360 nm and a strong, broad green emission peak at 530 nm. The two peaks are assigned to band-edge emission and oxygen-vacancy related defect emission. The emission intensity of ZnO and ZnO:TMAH nanocrystals was much lower than that of ZnO:MEA, which could be ascribed to PL quenching [39].

### 3.2. Effects of acid and base modification on dispersibility and stability of ZnO nanoink

To investigate the effects of acid/base modification on the dispersibility of inks, dynamic light scattering was performed. The diameters (figure S2) of ZnO, ZnO:MEA, and ZnO:TMAH were 22.5, 8.0, and 21.2 nm, respectively. We found the diameter of ZnO:MEA was nearly the same as the crystal size, apparently suggesting the ZnO:MEA nanoparticles were monodispersed. Meanwhile, we found over 80% of the ZnO:MEA nanoparticles were monodispersed based on the histogram size. However, ZnO:TMAH showed serious aggregation, with diameters ranging from 10.0 to 80.0 nm. According

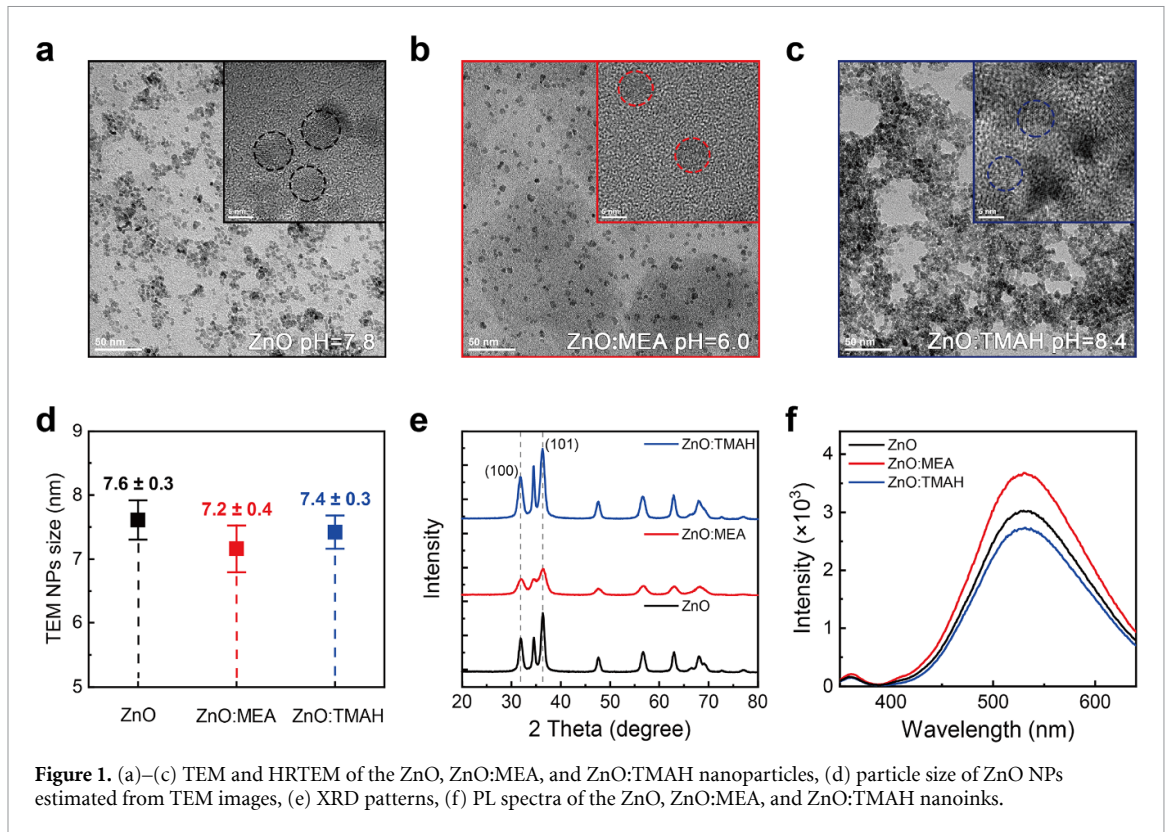


**Figure 1.** (a)–(c) TEM and HRTEM of the ZnO, ZnO:MEA, and ZnO:TMAH nanoparticles, (d) particle size of ZnO NPs estimated from TEM images, (e) XRD patterns, (f) PL spectra of the ZnO, ZnO:MEA, and ZnO:TMAH nanoinks.

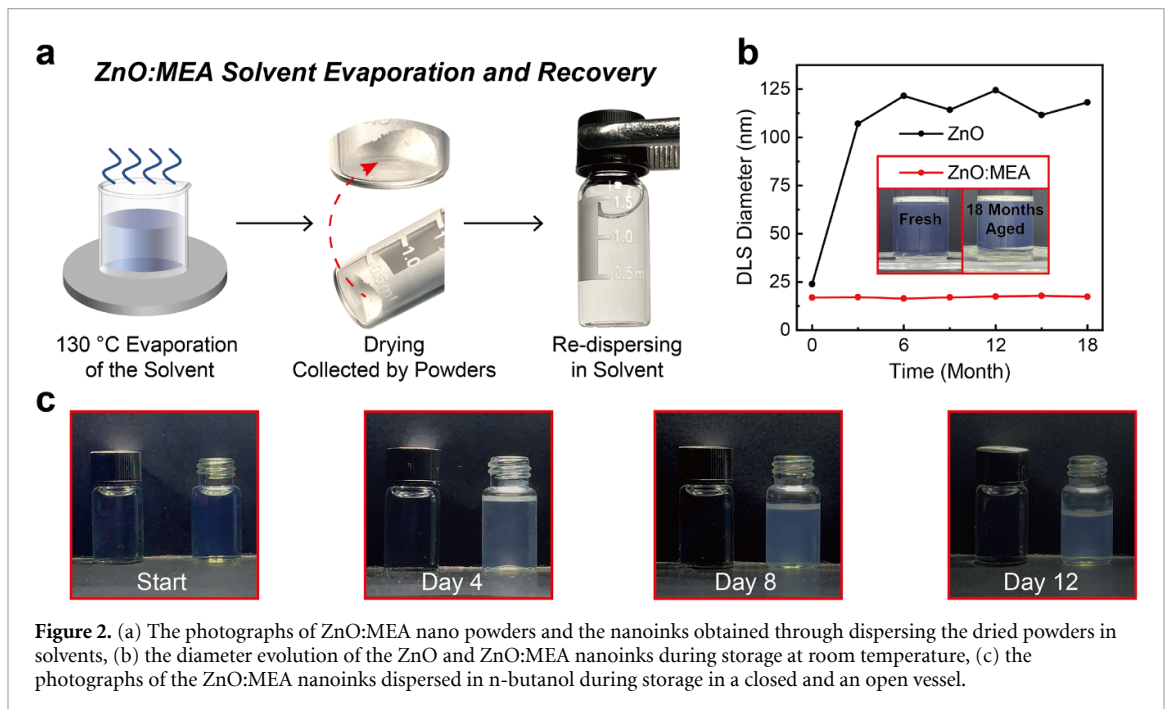


**Figure 2.** (a) The photographs of ZnO:MEA nano powders and the nanoinks obtained through dispersing the dried powders in solvents, (b) the diameter evolution of the ZnO and ZnO:MEA nanoinks during storage at room temperature, (c) the photographs of the ZnO:MEA nanoinks dispersed in n-butanol during storage in a closed and an open vessel.

to Ostwald Ripening theory [40], the inks with narrower diameter distributions were more difficult to form large particles, which is conducive to stabilizing nanoinks. On this basis, the ZnO:MEA ink would be more stable. Meanwhile, it is worth noting that the ZnO:MEA nanoparticles were also well dispersed in several solvents, including ethanol, IPA, n-butanol, and 2-methoxy ethanol (figure S3). Additionally, the ZnO:MEA inks could be dried and stored as powders

which could be redispersed in several solvents to form inks again (figure 2(a)). The excellent dispersibility of ZnO:MEA nano powders in various solvents makes them convenient for storage and transportation. The superior dispersibility and ink stability of ZnO:MEA were mainly ascribed to the removal of hydroxyl groups and steric stabilizing effect of MEA [41].

During real R2R printing, ink stability is essential for printing reproducibility, because inks are used

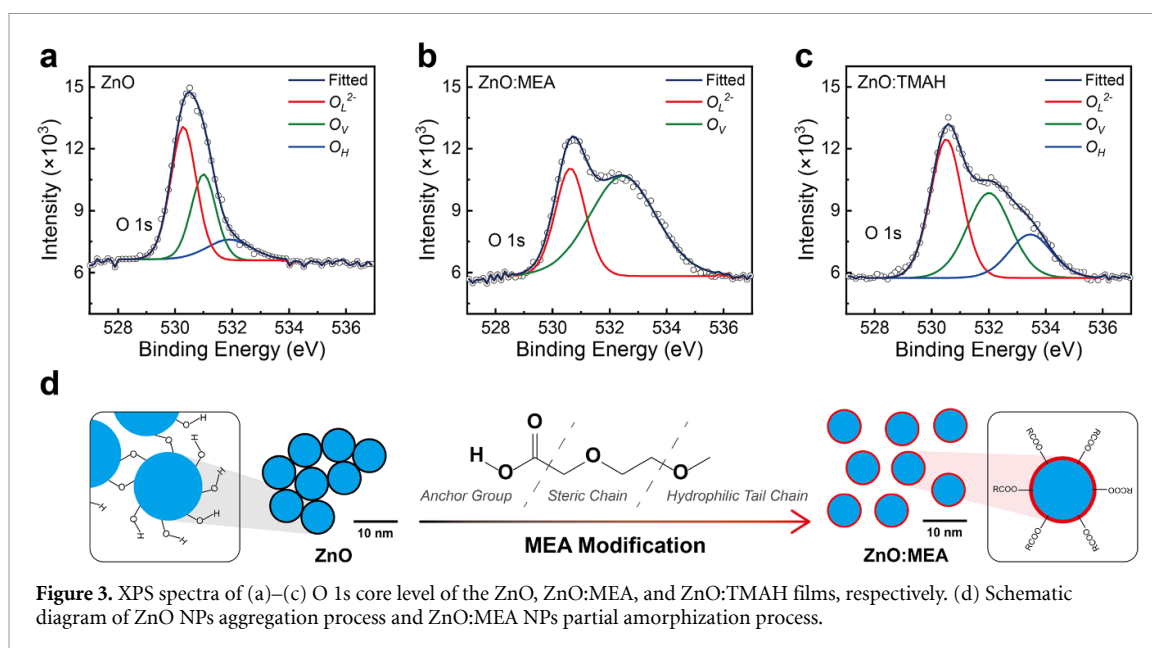


**Figure 3.** XPS spectra of (a)–(c) O 1s core level of the ZnO, ZnO:MEA, and ZnO:TMAH films, respectively. (d) Schematic diagram of ZnO NPs aggregation process and ZnO:MEA NPs partial amorphization process.

continuously at room temperature. Thus, we investigated the ink stability by storing these ZnO inks in the ambient atmosphere for several months, and photographs of ZnO and ZnO:MEA nanoinks were exhibited in figure S4. The pristine ZnO nanoink became turbid after one week storage in air. Obvious sediments formed in the ZnO:TMAH nanoinks after 2 h of storage. However, the ZnO:MEA nanoinks remained transparent after 18 months of storage (figure 2(b)), showing excellent stability. Herein, the improvement of stability came from the neutralization of hydroxyl groups, which was confirmed by the XPS result (*vide infra*). During R2R printing, inks are always placed in an open or half-open vessel, making it much easier to agglomerate during continuous printing because of solvent evaporation. Furthermore, to simulate the R2R printing, the ink stability in an open vessel was also studied. For continuous R2R printing, a high-boiling solvent should be used to avoid quick evaporation of solvent. Therefore, *n*-butanol was used as the dispersing solvent to investigate the ink stability in open vessels. Figure 2(c) shows the photographs of these nanoinks stored in a closed and open vessel at room temperature. After 12 days, the ZnO:MEA inks remained clear without obvious agglomeration, even though the solvent has evaporated by 1/3, which meant that ZnO:MEA had good stability in an open-air environment.

These observations indicated the MEA-modified ZnO was monodispersed and would be long-term stable during long-term storage and continuous printing process. Nevertheless, TMAH-modified ZnO was significantly aggregated. To gain more insight into the reasons, the XPS spectra of these films were investigated. Compared with the pristine ZnO films (figure S5, table S1), ZnO 2*p* core level for

ZnO:MEA and ZnO:TMAH films has 0.1 and 0.3 eV peaks shifted towards a lower binding energy direction, suggesting both acid and base additives have changed the coordination of Zn [42]. On the side of the O1s core level, we found the high-resolution O1s spectra of ZnO could be fitted by three Gaussian peaks (as shown in figures 3(a)–(c)). The low-binding energy  $O_L$  peak at 530.3 eV attributed to ZnO lattice oxygen [43]. The medium-binding energy  $O_V$  peak at 531.4 eV was attributed to oxygen-defect. And the high-binding energy peaks were from chemisorbed oxygen such as hydroxyl. Among these three peaks, the medium binding energy  $O_V$  peak in the ZnO:MEA film at 532.3 eV was not only associated with oxygen vacancies but also related with oxygen in MEA. For the ZnO film, the proportion of  $O_H$  peak at 531.9 eV was 14.38%. For the ZnO:MEA film, the hydroxyl groups were neutralized, which could not be detected in the ZnO:MEA film. For the ZnO:TMAH film, the proportion of  $O_H$  increased to 22.24% (summarized in table S2), and the peaks were shifted towards higher binding energy as well. The changes of  $O_H$  peaks indicated the TMAH addition aggravated the hydroxyl groups of ZnO film [31], while the treatment of MEA reduced the surface hydroxyl groups.

Based on the above results, a schematic diagram of aggregation and disaggregation processes of ZnO NPs was shown in figure 3(d). Dehydration between hydroxyl groups can push the formation of strong binding between ZnO nanoparticles, which is the main reason for agglomeration, consequently, the inks gradually become cloudy. In contrast, the MEA addition could remove the surface hydroxyl groups through Lewis acid-base reactions and break the aggregation. As an excellent steric stabilizer, MEA

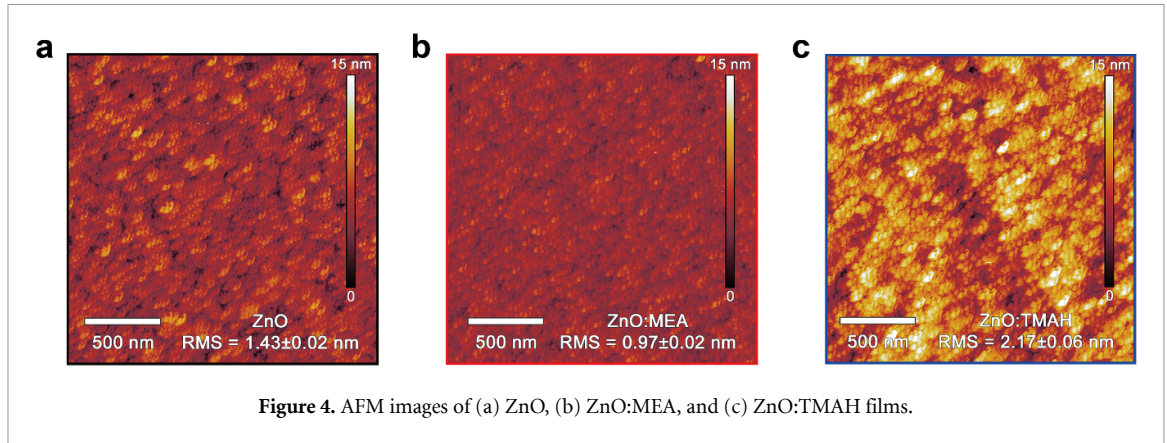


Figure 4. AFM images of (a) ZnO, (b) ZnO:MEA, and (c) ZnO:TMAH films.

may have three functions: (a) reacts with hydroxyl groups and breaks the aggregation; (b) enhances steric hindrance, making the ZnO NPs stable [36, 37], and (c) provides good alcohol solubility, which ensures excellent dispersibility of ZnO NPs in different alcohols. Therefore, the removal of hydroxyl groups and enhanced steric hindrance between nanoparticles contributed to excellent ink stability and dispersibility.

### 3.3. Application of acid and base modified ZnO NPs in OSCs

As ETLs, the film quality and surface morphology of ZnO films will highly influence the interface contact and interface charge transport. Thus, the film quality of ZnO ETL is significantly important for device performance and stability of OSCs. AFM images shown in figures 4(a)–(c) were performed to characterize the ZnO films. The root mean square (RMS) roughness values of ZnO, ZnO:MEA, and ZnO:TMAH films were  $1.43 \pm 0.02$ ,  $0.97 \pm 0.02$ , and  $2.17 \pm 0.06$  nm, respectively. Though the surface roughness of these films is not high, the ZnO:MEA film is still much smoother than the ZnO and ZnO:TMAH films. The ultra-smooth ZnO:MEA films with much smaller RMS relative to ZnO and ZnO:TMAH films were due to the excellent dispersibility of the ZnO:MEA nanoinks, which could be beneficial for charge transport between ETL and the active layer. The electron-only devices (Al/ZnO/Al or Al/ZnO:MEA/Al) were taken to study the electron-transporting properties of the ZnO and ZnO:MEA ETLs by space-charge-limited current (SCLC) measurement. The  $J$ – $V$  curves (figure S6) agreed with SCLC mode where there was an ohmic contact region and an SCLC region. Because of the trap-free SCLC behaviour of these devices, trapped space-charge regions did not exist. From the SCLC region, the electron mobilities of ZnO and ZnO:MEA ETLs can be estimated. According to the Mott–Gurney SCLC equation [44, 45]:

$$J = \frac{9}{8} \varepsilon_r \varepsilon_0 \mu \frac{V^2}{d^3}$$

where  $\varepsilon_r$ ,  $\varepsilon_0$ ,  $\mu_e$ , and  $d$  is the relative dielectric constants, the vacuum dielectric constant, electron mobility, and thickness, respectively. The electron mobilities of the ZnO and ZnO:MEA ETLs were calculated to be about  $8.68 \times 10^{-4}$  and  $8.35 \times 10^{-4} \text{ cm}^2 \text{ V}^{-1} \text{ S}^{-1}$ , respectively. The results agreed well with the theoretical electron mobility of ZnO ETL ( $10^{-4}$ – $10^{-3} \text{ cm}^2 \text{ V}^{-1} \text{ S}^{-1}$ ) [17, 26, 46, 47]. The electron mobilities indicated that acid modification has a detrimental effect on the conduction of ZnO NPs. Nevertheless, the SCLC regions were at a high bias region, in which the film traps were filled by the injected current. As exhibited in figure S6, the current density of the electron-only devices based on pristine ZnO ETL was lower compared to the ZnO:MEA one, which means there was higher trap density in the pristine ZnO ETL.

Figure 5(a) showed the device structure of ZnO and ZnO:MEA ETLs-based OSCs and the molecular structures of PM6 and Y6. The  $J$ – $V$  characteristics, EQE spectra, and integral currents of the OSCs were exhibited in figures 5(b) and (c). Table 1 lists the corresponding OSCs performance parameters. The OSCs based on ZnO ETL exhibited  $V_{OC}$ ,  $J_{SC}$ , fill factor (FF), and PCE of 0.842 V, 26.04  $\text{mA cm}^{-2}$ , 74.99%, and 16.47%, respectively. With MEA addition into ZnO, the device performance gradually improved first and then decreased, with 0.5  $\text{mg ml}^{-1}$  as a saturation (shown in table S3). As an optimization, PCE of 16.51% with  $V_{OC}$  of 0.842 V,  $J_{SC}$  of 25.81  $\text{mA cm}^{-2}$ , and FF of 75.06% was obtained. Such performance was among the highest efficiency of PM6:Y6 devices with an inverted structure [14, 27, 33]. But overall, the device performance was slightly influenced by MEA as the concentration of MEA was restricted within 2  $\text{mg ml}^{-1}$ . Further increasing the MEA concentration from 2 to 5  $\text{mg ml}^{-1}$  led to an obvious decrease in  $J_{SC}$  and PCE. Although the ZnO and ZnO:MEA ETL-based OSCs gave similar performance when the thickness was approximately 30 nm, the ZnO:MEA devices showed a high working thickness and large thickness tolerance. As exhibited in figure 5(b) and table 1, the ZnO ETL-based OSCs showed a rapid drop in performance when the

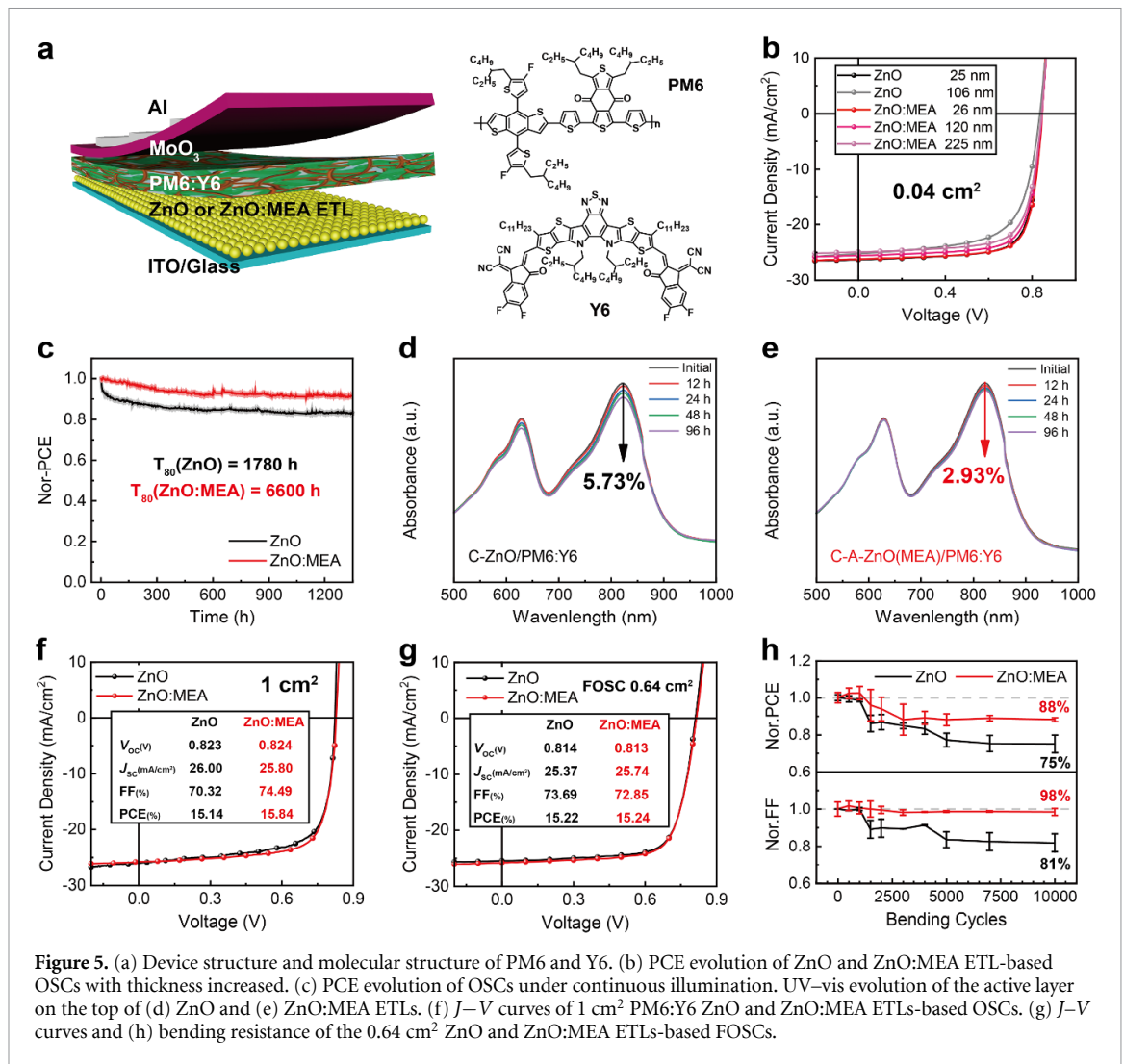


**Figure 5.** (a) Device structure and molecular structure of PM6 and Y6. (b) PCE evolution of ZnO and ZnO:MEA ETL-based OSCs with thickness increased. (c) PCE evolution of OSCs under continuous illumination. UV-vis evolution of the active layer on the top of (d) ZnO and (e) ZnO:MEA ETLs. (f)  $J$ - $V$  curves of 1 cm<sup>2</sup> PM6:Y6 ZnO and ZnO:MEA ETLs-based OSCs. (g)  $J$ - $V$  curves and (h) bending resistance of the 0.64 cm<sup>2</sup> ZnO and ZnO:MEA ETLs-based FOSCs.

thickness of ZnO ETL increased from 25 to 213 nm. In contrast, the performance of the ZnO:MEA ETL-based OSCs was still higher than 15% when the thickness of ZnO:MEA ETL increased from 26 to 225 nm, which indicated ZnO:MEA ETL was more applicable to large-area printing owing to its good conductivity and proper film quality. The high thickness tolerance of ZnO:MEA mainly benefited from the improved film quality since the monodispersed nanoinks would enable a more compact and smoother film. Such a large work thickness would reduce printing difficulties and improve reproducibility.

Figure 5(c) shows the evolution of PCE under continuous illumination. The OSCs with ZnO ETL showed a quick burn-in degradation within 20 h and a relatively slower degradation as time increased from 20 to 1200 h. The PCE remained at 83% after 1350 h. Encouragingly, the burn-in degradation of the ZnO:MEA devices was greatly inhibited, thereby the device degradation was much slower, retaining 92% of the initial value after 1350 h of degradation. Consequently, the  $T_{80}$  lifetimes of the ZnO and ZnO:MEA devices were estimated approx. 1780 and 6600 h, respectively (figure S7). The dramatically

**Table 2.** Device performance of the rigid (1 cm<sup>2</sup>) and flexible (0.64 cm<sup>2</sup>) inverted OSCs employed ZnO and ZnO:MEA ETLs.

Device area (cm <sup>2</sup> )	ETL	Thickness (nm)	V <sub>OC</sub> (V)	J <sub>SC</sub> (mA cm <sup>-2</sup> )	FF (%)	<sup>a</sup> PCE (%)	<sup>b</sup> PCE (%)
Rigid	ZnO	25 ± 3.4	0.823	26.00	70.32	15.05 ± 0.12	15.14
1.00 cm <sup>2</sup>	ZnO:MEA	26 ± 5.1	0.824	25.80	74.40	15.81 ± 0.06	15.84
Flexible	ZnO	52 ± 6.7	0.814	25.37	73.69	15.22 ± 0.04	15.26
0.64 cm <sup>2</sup>	ZnO:MEA	53 ± 5.1	0.813	25.74	72.85	15.24 ± 0.06	15.31

<sup>a</sup> Average PCE was calculated from ten individual devices.

<sup>b</sup> The maximum PCE of the ten individual devices.

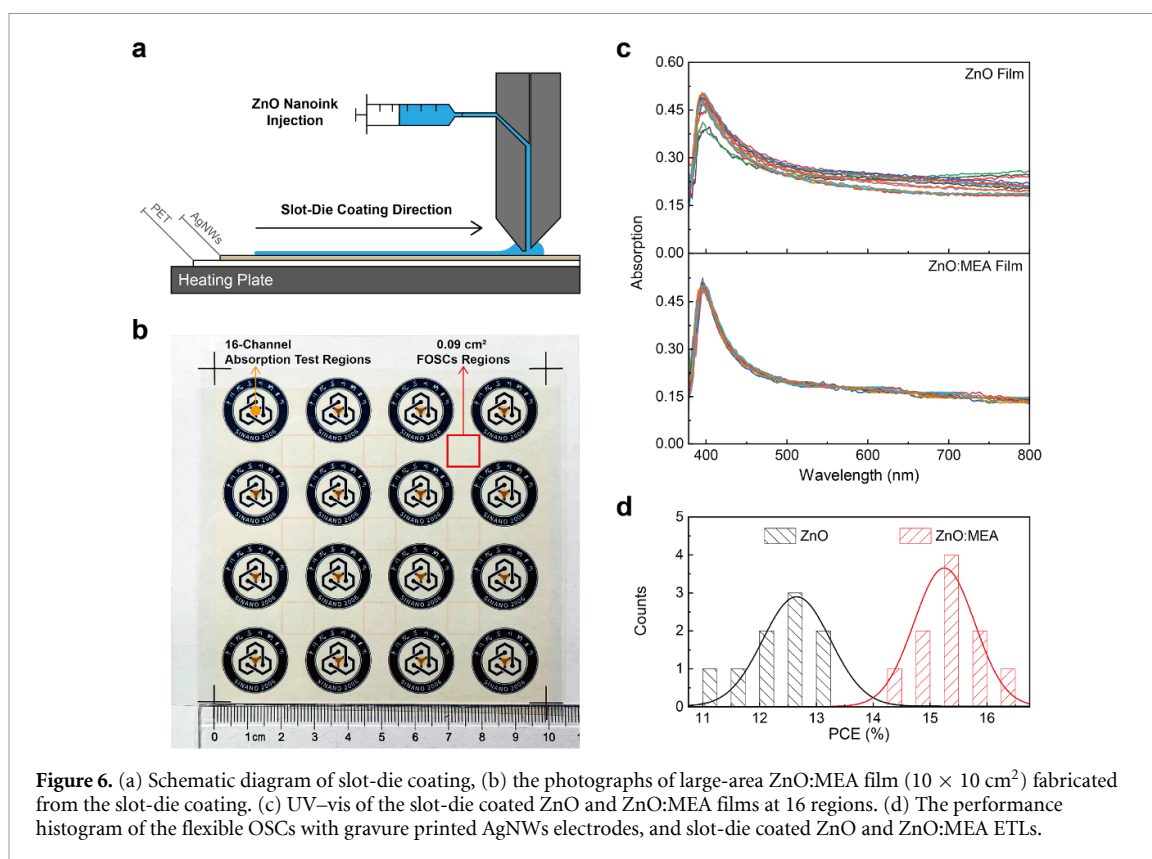
difference demonstrated the significant effect of ZnO ETL on the degradation process. Considering that average annual solar irradiation from 2011 to 2020 in Suzhou (Jiangsu Province, China) was 1950 h (figure S8) [48], a continuous lifetime of 6600 h for the ZnO:MEA ETL-based OSCs indicated that the OSCs could work for at least longer than three years, meeting the requirements of some consumer electronics. Previous studies have proved that interface degradation due to the catalytic effect of the ZnO ETL was the main reason for device degradation. The existence of hydroxyl groups would accelerate the surface degradation due to the generation of hydroxyl radicals through photo-oxidation of hydroxyl groups [27]. The hydroxyl radical is the reactive species that decompose the organic non-fullerene acceptors [31]. Based on the absorption absorbance of the ETL/PM6:Y6 films (figures 5(d) and (e)), we observed the decrease in the absorption intensity at around 820 nm for ZnO:MEA/PM6:Y6 films was slower than that of ZnO/PM6:Y6 films, which indicated that photobleaching reactions between ZnO and active layer were eliminated with MEA addition into ZnO. In ZnO:MEA ETL, reaction between acid and hydroxyl groups could effectively remove the hydroxyl groups, which has been proved by the XPS spectra.

When device area increased to 1 cm<sup>2</sup>, the ZnO:MEA ETL-based OSCs (As shown in table 2) got a PCE of 15.84%, with V<sub>OC</sub>, J<sub>SC</sub>, and FF of 0.824 V, 25.80 mA cm<sup>-2</sup>, and 74.49%, respectively. Devices with ZnO ETL exhibited an inferior performance of 15.14% (figure 5(f)). This result strongly suggested that ultra-smooth films and the removal of hydroxy-oxygen defects in ETLs have great advantages in large-area devices. The integrated current density calculated from EQE spectra (figure S9) agreed with J–V characteristics. To deeply understand the reason of performance improvement for the 1 cm<sup>2</sup> devices, the light intensity-dependent V<sub>OC</sub> and J<sub>SC</sub> of these devices were measured and shown in figure S10(a) and (b). This result suggested bimolecular recombination and space charge effects were negligible in all OSCs [49, 50]. Regarding the light intensity-dependent V<sub>OC</sub>, a slope of  $nk_B T/q$  could be expected where  $n$ ,  $k_B$ ,  $T$ , and  $q$  are the ideal factor, Boltzmann constant, absolute temperature, and elementary charge, respectively [51]. The slopes of OSCs with ZnO and ZnO:MEA ETL shown in

figure S10(b) were estimated to be 1.32  $k_B/q$  and 1.15  $k_B/q$ . The slope of ZnO ETL-based OSCs is larger than that of ZnO:MEA ETL-based ones, suggesting that more trap-assisted recombination has occurred [51]. Because the device structure are the same except ETL, there is a higher defect-assisted recombination in the ZnO-based OSCs, probably due to recombination between ZnO and organic layers. From EIS shown in figure S10(c), transporting resistances of the ZnO and ZnO:MEA-involved OSCs were 6.7 and 2.7  $\Omega$ , while the recombination resistance was 28.1 and 95.6  $\Omega$ . The lower transport resistance and much higher recombination resistance contributed to better performance of the ZnO:MEA ETL-based large-area device.

Meanwhile, ZnO:MEA ETL was utilized in FOSCs (0.64 cm<sup>2</sup>). FOSCs with structure of PET/AgNWs/ $\alpha$ -ZnO/ZnO or ZnO:MEA ETL/PM6:Y6/MoO<sub>3</sub>/Al were fabricated. Here,  $\alpha$ -ZnO was an amorphous ZnO layer, which was used to modify the AgNWs electrodes [9]. As shown in figures 5(g) and (h), the ZnO and ZnO:MEA ETL-based flexible PM6:Y6 OSCs with an area of 0.64 cm<sup>2</sup> showed a similar performance of around 15.30%. However, ZnO:MEA ETL-based FOSCs exhibited much better mechanical flexibility than ZnO ETL-based ones. Bending resistance of these FOSCs was investigated using a bending machine, as shown in figure S11. After 10 000 bending cycles which bending radius was 5.0 mm, ZnO-based FOSCs maintained 75%, while ZnO:MEA ones maintained 88%. The main reason for the performance degradation during bending was ascribed to the decrease of FF, implying that the main reason was interface degradation. Therefore, the enhanced bending resistance undoubtedly proved that a compact and smooth ZnO ETL was significantly important for the mechanical properties of FOSCs.

The monodispersed ZnO:MEA nanoparticles ensured excellent dispersibility, long-term stability, large working thickness, and ultra-smooth ETL films, demonstrating the great potential of the ZnO:MEA nanoinks in large-area printing. To evaluate the possibility of printing, we fabricated large-area ZnO:MEA films through slot-die coating (figure 6(a)) with gravure-printed PET/AgNWs as cathode [52]. ZnO and ZnO:MEA nanoinks (60 mg ml<sup>-1</sup>) for slot-die coating were dispersed in n-butanol. Firstly,



the viscosity of ZnO and ZnO:MEA nanoinks were determined to be 4.70 and 3.21 mPa s, respectively. Since the addition amount of MEA is low, the addition of MEA had a negligible influence on inks viscosity. Figure 6(b) showed photographs of large-area ( $10 \times 10 \text{ cm}^2$ ) slot-die coated films. We found that large-area AgNW/ZnO:MEA films had good optical transparency. Furthermore, the homogeneity of the large-area films was investigated by testing the absorption spectra using a homemade multichannel photometer. As shown in figure 6(c), it was obvious to find that the absorption spectra of ZnO:MEA films at 16 regions were nearly the same, indicating excellent film uniformity. And according to the AFM images (figure S12), the RMS values of slot-die coated ZnO and ZnO:MEA films were  $6.0 \pm 1.2$  and  $3.0 \pm 0.7$  nm, respectively. On top of the large-area AgNWs electrode and ZnO:MEA ETLs, the active layer, and Al electrode were prepared sequentially through spin-coating and vacuum deposition to form FOSCs ( $0.09 \text{ cm}^2$ ). Table S5 lists the parameters of these FOSCs. The histogram of performance (figure 6(d)) showed that the FOSCs with slot-die coated ZnO:MEA ETL exhibited an average efficiency approximately 15.22% and a highest performance of 16.27%, which were much higher than those devices with slot-die coated ZnO ETL [53].

#### 4. Conclusions

All in all, we studied the effects of pH environment on dispersibility and long-term stability of ZnO

nanoinks. The utilization of a base (TMAH) introduced excess hydroxyl radicals and accelerated the aggregation of nanoparticles. In contrast, the use of an acid (MEA) additive resulted in monodispersed ZnO nanoparticles and excellent ink stability, which remained stable for more than 18 months at room temperature or re-disperse to form inks after drying. The monodispersed ZnO nanoinks improved the film quality, and ultra-smooth ZnO films with a high working thickness of at least 200 nm were obtained. Particularly, for the  $1 \text{ cm}^2$  large-area OSCs, the ZnO:MEA ETL-based PM6:Y6 OSCs exhibited a PCE up to 15.84%. Because of the removal of surface hydroxy groups, the ZnO:MEA-based OSCs exhibited significantly improved long-term stability (up to 6600 h of  $T_{80}$  lifetime) compared with the ZnO-based ones ( $T_{80}$  lifetime of approximately 1780 h). Additionally, the excellent monodispersibility and thickness independence ensured high-quality large-area ( $10 \times 10 \text{ cm}^2$ ) films by slot-die coating. This work provided an easy way to simultaneously solve the ink stability and film defect issues, which also improved the performance and long-term stability of non-fullerene acceptor OSCs.

#### Data availability statement

All relevant data are within the paper and its supporting information files.

All data that support the findings of this study are included within the article (and any supplementary files).

## Acknowledgments

This work was financially supported by the National Natural Science Foundation of China (51773224), Youth Innovation Promotion Association, CAS (2019317), Vacuum Interconnected Nanotech Workstation, SINANO, CAS.

## Conflict of interest

No known competing financial interests or personal relationships.

## Ethics statement

The study was approved by Shanghai University and SINANO, CAS.

## ORCID iDs

Qun Luo  <https://orcid.org/0000-0002-7527-460X>  
Chang-Qi Ma  <https://orcid.org/0000-0002-9293-5027>

## References

- [1] Wang J, Zheng Z, Zu Y, Wang Y, Liu X, Zhang S, Zhang M and Hou J 2021 A tandem organic photovoltaic cell with 19.6% efficiency enabled by light distribution control *Adv. Mater.* **33** e2102787
- [2] Zhang M et al 2021 Single-layered organic photovoltaics with double cascading charge transport pathways: 18% efficiencies *Nat. Commun.* **12** 309
- [3] Lin Y et al 2020 Self-assembled monolayer enables hole transport layer-free organic solar cells with 18% efficiency and improved operational stability *ACS Energy Lett.* **5** 2935
- [4] Zhan L, Li S, Xia X, Li Y, Lu X, Zuo L, Shi M and Chen H 2021 Layer-by-layer processed ternary organic photovoltaics with efficiency over 18% *Adv. Mater.* **33** 2007231
- [5] Li C et al 2021 Non-fullerene acceptors with branched side chains and improved molecular packing to exceed 18% efficiency in organic solar cells *Nat. Energy* **6** 605
- [6] Hau S K et al 2008 Air-stable inverted flexible polymer solar cells using zinc oxide nanoparticles as an electron selective layer *Appl. Phys. Lett.* **92** 253301
- [7] Moussodia R O et al 2010 Biocompatible and stable ZnO quantum dots generated by functionalization with siloxane-core PAMAM dendrons *J. Mater. Chem.* **20** 1147
- [8] Krebs F C et al 2008 A simple nanostructured polymer/ZnO hybrid solar cell-preparation and operation in air *Nanotechnology* **19** 424013
- [9] Pan W et al 2021 An efficiency of 14.29% and 13.08% for 1 cm<sup>2</sup> and 4 cm<sup>2</sup> flexible organic solar cells enabled by sol-gel ZnO and ZnO nanoparticle bilayer electron transporting layers *J. Mater. Chem. A* **9** 16889
- [10] Zhang S, Wang H, Duan X, Rao L, Gong C, Fan B, Xing Z, Meng X, Xie B and Hu X 2021 Printable and homogeneous NiO<sub>x</sub> hole transport layers prepared by a polymer layersiloxane-core PAMAM dendrons as an electron selective layer *Adv. Funct. Mater.* **31** 2106495
- [11] Ji G, Zhao W, Wei J, Yan L, Han Y, Luo Q, Yang S, Hou J and Ma C-Q 2019 12.88% efficiency in doctor-blade coated organic solar cells through optimizing the surface morphology of a ZnO cathode buffer layer *J. Mater. Chem. A* **7** 212
- [12] Li Y et al 2015 Ambient stable large-area flexible organic solar cells using silver grid hybrid with vapor phase polymerized poly(3,4-ethylenedioxythiophene) cathode *Sol. Energy Mater. Sol. Cells* **143** 354
- [13] Hamsch M et al 2014 Improved stability of non-ITO stacked electrodes for large area flexible organic solar cells *Sol. Energy Mater. Sol. Cells* **130** 182
- [14] Lee W et al 2020 High colloidal stability ZnO nanoparticles independent on solvent polarity and their application in polymer solar cells *Sci. Rep.* **10** 18055
- [15] Wu N, Luo Q, Bao Z, Lin J, Li Y-Q and Ma C-Q 2015 Zinc oxide: conjugated polymer nanocomposite as cathode buffer layer for solution processed inverted organic solar cells *Sol. Energy Mater. Sol. Cells* **141** 248
- [16] Wei J F, Zhang C, Ji G, Han Y, Ismail I, Li H, Luo Q, Yang J and Ma C-Q 2019 Roll-to-roll printed stable and thickness-independent ZnO:PEI composite electron transport layer for inverted organic solar cells *Sol. Energy* **193** 102
- [17] Wei J, Ji G, Zhang C, Yan L, Luo Q, Wang C, Chen Q, Yang J, Chen L and Ma C-Q 2018 Silane-capped ZnO nanoparticles for use as the electron transport layer in inverted organic solar cells *ACS Nano* **12** 5518
- [18] Yi M B et al 2020 Facile preparation of a polymer-ZnO composite colloid as an electron transport layer and its effects on inverted polymer solar cells *J. Phys. Chem. Solids* **145** 109538
- [19] Ambade S B, Ambade R B, Lee W, Mane R S, Yoon S C and Lee S-H 2014 Development of highly transparent seedless ZnO nanorods engineered for inverted polymer solar cells *Nanoscale* **6** 12130
- [20] Ambade S B et al 2016 Co-functionalized organic/inorganic hybrid ZnO nanorods as electron transporting layers for inverted organic solar cells *Nanoscale* **8** 5024
- [21] Chen S, Small C E, Amb C M, Subbiah J, Lai T-H, Tsang S-W, Manders J R, Reynolds J R and So F 2012 Inverted polymer solar cells with reduced interface recombination *Adv. Energy Mater.* **2** 1333
- [22] Lee B R et al 2014 Amine-based polar solvent treatment for highly efficient inverted polymer solar cells *Adv. Mater.* **26** 494
- [23] Polydorou E et al 2017 Avoiding ambient air and light induced degradation in high-efficiency polymer solar cells by the use of hydrogen-doped zinc oxide as electron extraction material *Nano Energy* **34** 500
- [24] Bai S et al 2015 Ethanedithiol treatment of solution-processed ZnO thin films: controlling the intragap states of electron transporting interlayers for efficient and stable inverted organic photovoltaics *Adv. Energy Mater.* **5** 1401606
- [25] Fu P, Guo X, Zhang B, Chen T, Qin W, Ye Y, Hou J, Zhang J and Li C 2016 Achieving 10.5% efficiency for inverted polymer solar cells by modifying the ZnO cathode interlayer with phenols *J. Mater. Chem. A* **4** 16824
- [26] Zhu X Q et al 2019 Surface modification of ZnO electron transport layers with glycine for efficient inverted non-fullerene polymer solar cells *Org. Electron.* **70** 25
- [27] Han Y et al 2021 An efficiency of 16.46% and a T<sub>80</sub> lifetime of over 4000 h for the PM6: Y6 inverted organic solar cells enabled by surface acid treatment of the zinc oxide electron transporting layer *ACS Appl. Mater. Interfaces* **13** 17869
- [28] Ischenko V, Polarz S, Grote D, Stavarache V, Fink K and Driess M 2005 Zinc oxide nanoparticles with defects *Adv. Funct. Mater.* **15** 1945
- [29] Guang S, Yu J, Wang H, Liu X, Qu S, Zhu R and Tang W 2021 A low temperature processable tin oxide interlayer via amine-modification for efficient and stable organic solar cells *J. Energy Chem.* **56** 496
- [30] Chen R et al 2019 High-efficiency, hysteresis-less, UV-stable perovskite solar cells with cascade ZnO-ZnS electron transport layer *J. Am. Chem. Soc.* **141** 541
- [31] Liu B, Han Y, Li Z, Gu H, Yan L, Lin Y, Luo Q, Yang S and Ma C-Q 2020 Visible light-induced degradation of inverted polymer: nonfullerene acceptor solar cells: initiated by the light absorption of ZnO layer *Sol. RRL* **5** 2000638

- [32] Liu H, Liu Z-X, Wang S, Huang J, Ju H, Chen Q, Yu J, Chen H and Li C-Z 2019 Boosting organic-metal oxide heterojunction via conjugated small molecules for efficient and stable nonfullerene polymer solar cells *Adv. Energy Mater.* **9** 1900887
- [33] Cheng H-W et al 2020 Potassium-presenting zinc oxide surfaces induce vertical phase separation in fullerene-free organic photovoltaics *Nano. Lett.* **20** 715
- [34] Bian S W, Mudunkotuwa I A, Rupasinghe T and Grassian V H 2011 Aggregation and dissolution of 4 nm ZnO nanoparticles in aqueous environments: influence of pH, ionic strength, size, and adsorption of humic acid *Langmuir* **27** 6059
- [35] Mohd Omar F, Abdul Aziz H and Stoll S 2014 Aggregation and disaggregation of ZnO nanoparticles: influence of pH and adsorption of suwannee river humic acid *Sci. Total Environ.* **468–469** 195
- [36] Linse P and Lobaskin V 2000 Electrostatic attraction and phase separation in solutions of like-charged colloidal particles *J. Chem. Phys.* **112** 3917
- [37] Bostrom M, Deniz V, Franks G V and Ninham B W 2006 Extended DLVO theory: electrostatic and non-electrostatic forces in oxide suspensions *Adv. Colloid Interface Sci.* **123–126** 5
- [38] Khenkin M V et al 2020 Consensus statement for stability assessment and reporting for perovskite photovoltaics based on ISOS procedures *Nat. Energy* **5** 35
- [39] Yang Y, Zou T, Zhao R, Kong Y, Su L, Ma D, Xiao X and Wang Y 2021 Fluorescence 'turn-on' probe for Al<sup>3+</sup> detection in water based on ZnS/ZnO quantum dots with excellent selectivity and stability *Nanotechnology* **32** 375001
- [40] Bastus N G, Comenge J and Puentes V 2011 Kinetically controlled seeded growth synthesis of citrate-stabilized gold nanoparticles of up to 200 nm: size focusing versus ostwald ripening *Langmuir* **27** 11098
- [41] Wu L, Zhang J and Watanabe W 2011 Physical and chemical stability of drug nanoparticles *Adv. Drug Deliv. Rev.* **63** 456
- [42] Ren T, Li L, Cai X, Dong H, Liu S and Li Y 2012 Engineered polyethylenimine/graphene oxide nanocomposite for nuclear localized gene delivery *Polym. Chem.* **3** 2561
- [43] Chen M, Wang X, Yu Y H, Pei Z L, Bai X D, Sun C, Huang R F and Wen L S 2000 X-ray photoelectron spectroscopy and auger electron spectroscopy studies of Al-doped ZnO films *Appl. Surf. Sci.* **158** 134
- [44] Fröhlich H 1949 Electronic processes in ionic crystals *Nature* **164** 377
- [45] Barbe D F 1971 Space-charge-limited current enhanced by Frenkel effect *J. Phys. D: Appl. Phys.* **4** 1812
- [46] Liao S-H, Jhuo H-J, Yeh P-N, Cheng Y-S, Li Y-L, Lee Y-H, Sharma S and Chen S-A 2014 Single junction inverted polymer solar cell reaching power conversion efficiency 10.31% by employing dual-doped zinc oxide nano-film as cathode interlayer *Sci. Rep.* **4** 6813
- [47] Pan J, Chen J, Huang Q, Khan Q, Liu X, Tao Z, Zhang Z, Lei W and Nathan A 2016 Size tunable ZnO nanoparticles to enhance electron injection in solution processed QLEDs *ACS Photonics* **3** 215
- [48] Weather forecast and climate of Suzhou city, Jiangsu Province (available at: [www.weather-atlas.com/zh/china/suzhou-climate#daylight\\_sunshine](http://www.weather-atlas.com/zh/china/suzhou-climate#daylight_sunshine))
- [49] Cowan S R, Roy A and Heeger A J 2010 Recombination in polymer-fullerene bulk heterojunction solar cells *Phys. Rev. B* **82** 245207
- [50] Koster L J A, Mihailetchi V D, Xie H and Blom P W M 2005 Origin of the light intensity dependence of the short-circuit current of polymer/fullerene solar cells *Appl. Phys. Lett.* **87** 203502
- [51] Hawks S A, Li G, Yang Y and Street R A 2014 Band tail recombination in polymer: fullerene organic solar cells *J. Appl. Phys.* **116** 074503
- [52] Wang Z et al 2020 High power conversion efficiency of 13.61% for 1 cm<sup>2</sup> flexible polymer solar cells based on patternable and mass current of polymer/fullerene solar cells dual-doped z *Adv. Funct. Mater.* **31** 2007276
- [53] Cha H-C, Huang Y-C, Hsu F-H, Chuang C-M, Lu D-H, Chou C-W, Chen C-Y and Tsao C-S 2014 Performance improvement of large-area roll-to-roll slot-die-coated inverted polymer solar cell by tailoring electron transport layer *Sol. Energy Mater. Sol. Cells* **130** 191